

# Improving the Defect Tolerance of PBF-LB/M Processed 316L Steel by Increasing the Nitrogen Content

Felix Stern,\* Louis Becker, Chengsong Cui, Jochen Tenkamp, Volker Uhlenwinkel, Matthias Steinbacher, Johannes Boes, Jonathan Lentz, Rainer Fechte-Heinen, Sebastian Weber, and Frank Walther

Nitrogen (N) in steels can improve their mechanical strength by solid solution strengthening. Processing N-alloyed steels with additive manufacturing, here laser powder bed fusion (PBF-LB), is challenging as the N-solubility in the melt can be exceeded. This degassing of N counteracts its intended positive effects. Herein, the PBF-LB processed 316L stainless steel with increased N-content is investigated and compared to PBF-LB 316L with conventional N-content. The N is introduced into the steel by nitriding the powder and mixing it with the starting powder to achieve an N-content of approximately 0.16 mass%. Thermodynamic calculations for maximum solubility to avoid N outgassing and pore formation under PBF-LB conditions are performed beforehand. Based on the results, a higher defect tolerance under fatigue characterized by Murakami model can be achieved without negatively influencing the PBF-LB processability of the 316L steel. The increased N-content leads to higher hardness (+14%), yield strength (+16%), tensile strength (+9%), and higher failure stress in short time fatigue test (+16%).

(PBF-LB/M). Due to this, considerable knowledge regarding the microstructure and mechanical as well as chemical behavior and part/specimen densities of 99.9% or more have been reported. However, there is still a high scatter in the available data regarding the mechanical and especially the fatigue behavior and fatigue strength,<sup>[1,2]</sup> as these properties are strongly influenced by individual process parameters, building orientation, surface quality, porosity, and residual stresses. Due to this, it is well known that process-induced defects, even at a very small scale, are detrimental to fatigue life.<sup>[1,2]</sup> As those pores or lack of fusion (LoF) defects act as local stress raisers, the crack initiation is favored in their vicinity. If internal defects are present in the AM part, they can only be mitigated or even closed when applying posttreatment procedures such as hot-isostatic pressing (HIP).<sup>[3]</sup>

## 1. Introduction


The stainless steel AISI 316L (X2CrNiMo17-12-2, DIN 1.4404) is one of the most used Fe-based alloys for additive manufacturing (AM) by laser-based powder bed fusion processing of metals

Nonetheless, all postprocessing also leads to higher component costs as well as unintentional grain coarsening and dissolution of the process-induced cellular subgrain structure, which is mainly responsible for the high strength of the PBF-LB/M material compared to the conventional one.<sup>[4,5]</sup> However, fatigue strength of HIPed specimens in the low cycle fatigue regime is reduced, whereas it can improve the high cycle fatigue behavior.<sup>[1]</sup>

F. Stern, J. Tenkamp, F. Walther  
Chair of Materials Test Engineering (WPT)  
TU Dortmund University  
44227 Dortmund, Germany  
E-mail: felix.stern@tu-dortmund.de

L. Becker, J. Boes, J. Lentz, S. Weber  
Chair for Materials Technology (LWT)  
Ruhr University Bochum  
44801 Bochum, Germany

C. Cui, V. Uhlenwinkel, M. Steinbacher, R. Fechte-Heinen  
Materials Engineering Department  
Leibniz Institute for Materials Engineering-IWT  
28359 Bremen, Germany

 The ORCID identification number(s) for the author(s) of this article can be found under <https://doi.org/10.1002/adem.202200751>.

© 2022 The Authors. Advanced Engineering Materials published by Wiley-VCH GmbH. This is an open access article under the terms of the Creative Commons Attribution License, which permits use, distribution and reproduction in any medium, provided the original work is properly cited.

DOI: 10.1002/adem.202200751

Most of the results found in the literature show contradictory results regarding the fatigue behavior of AM parts compared to conventional material<sup>[2,6–8]</sup> or fatigue life suffers from high scatter.<sup>[9]</sup> The reason for this is that a lot of different material conditions with and without posttreatment are investigated. Especially, the as-built surface of AM specimens and internal defects are influencing the test results in a significant manner so that a direct comparison even of different conditions of the same material can be challenging. Beretta et al.<sup>[10]</sup> compared AM and conventionally manufactured parts from AlSi10Mg and Ti6Al4V, showing that high scatter of results for machined AM specimens is mostly linked to the presence of defects with different sizes. If this is considered, machined and stress relieved AM material under fatigue loading is either comparable or even better than conventional material. Murakami et al.<sup>[9]</sup> also addressed this topic and proposed a modified S–N curve based on the  $\sqrt{\text{area}}$ -model instead of the classical S–N curves. They state that scatter of fatigue results from specimens with defects

is caused due to each defect creating a single S–N curve. As there is in general a random scatter in the size of crack-initiating defects in PBF-LB specimens, the obtained S–N curves are based on data points of different individual defect-size dependent S–N curves. This is supported by the results of Kotzem et al.<sup>[11]</sup> where specimens from 316L with defined internal defect sizes were manufactured by PBF-LB/M and clearly distinguishable S–N curves could be found for each defect size.

Solid solution strengthening is often used to improve the strength of metals. In austenitic steels, carbon and nitrogen (N) are mostly used for interstitial solid solution strengthening because of it being one of the most effective strengthening mechanisms.<sup>[12]</sup> However, increasing the carbon content in austenitic CrNi steels promotes the formation of carbides, thus decreasing the corrosion resistance due to the reduction of dissolved Cr in the steel which is much less than the case for N (Cr<sub>23</sub>C<sub>6</sub> compared to CrN or Cr<sub>2</sub>N). N has multiple beneficial effects on Fe alloys when used as alloying element. It stabilizes the austenitic (γ-) phase<sup>[13]</sup> and, thus, can partly replace the expensive element Ni.<sup>[14]</sup> Furthermore, N promotes the metallic bonding character which leads to an increase in strength and ductility<sup>[15]</sup> and, additionally, improves corrosion resistance against intergranular, pitting, and crevice corrosion.<sup>[16]</sup> Alloys with up to 1 mass% of N are used for, e.g., medical applications.<sup>[17]</sup>

In PBF-LB/M, different strategies have already been used to increase the amount of nitrogen in steels. Powder modification was performed in terms of nitriding the powder to increase the N-content. Stern et al.<sup>[18]</sup> investigated the gas-nitrided steel powder X30CrMo7-2 and characterized the influence of the increased N-content of 0.68 mass% compared to the untreated material with 0.049 mass% of N on the mechanical compressive behavior. The N-content was reduced to 0.47 mass% after PBF-LB/M accompanied by high amount of gas pores in the processed steel. Nevertheless, hardness increased significantly, especially after tempering twice at 590 °C for 2 h. Compressive yield strength of tempered specimens was increased to 1990 MPa compared to specimens without increased N which only reached 1225 MPa in as-built condition. A prealloyed martensitic steel X30CrMoN15-1 was characterized by Boes et al.<sup>[19]</sup> which was gas atomized under N atmosphere and afterward processed by PBF-LB/M. N-content also decreased from powder to PBF-LB/M specimen from 0.18 to 0.14 mass% as the steel solidifies primary in the ferritic phase which results in a much lower N solubility. Here, as-built as well as heat-treated conditions were compared. The results from short time fatigue test procedure showed better fatigue behavior of the as-built condition due to higher ductility from retained austenite, thus, leading to higher defect tolerance under fatigue. Electron back scatter diffraction (EBSD) analysis revealed transformation of austenite to martensite in the vicinity of the fracture surface in combination with increase of hardness from 496 HV30 in the bulk as-built material up to 720 HV0.1 in the fatigue crack region. In situ interstitial alloying was investigated by Valente et al.<sup>[20]</sup> by processing 316L powder with additional 2.5 mass% Cr<sub>2</sub>N by PBF-LB/M. They achieved a N-content of 0.31 mass% accompanied by a hardness increase of about 40 HV0.1 and no measurable weight loss in FeCl<sub>3</sub> solution after 10 days of immersion regarding corrosion properties.

Boes et al.<sup>[16]</sup> aimed for interstitial solid solution strengthening by increasing the N-content by gas-nitriding the 316L powder

from 0.039 to 0.589 mass% exceeding the estimated maximum solubility of approximately 0.3 mass%. The higher N-content was found to be caused by the formation of fine nitrides on the surface and M(C,N) precipitates at the surface-near grain boundaries of the powder particles. The nitrided powder was mixed with the starting powder so that N contents of 0.065 and 0.27 mass% N in the mixed powder and 0.069 and 0.22 mass% N after PBF-LB were achieved. Specimens with 0.22 mass% N showed increased porosity with spherical pores, indicating the exceeding of the maximum solubility of nitrogen in the liquid phase while specimens with lower amount of nitrogen showed slightly increased N-content possibly caused by nitrogen uptake from the shielding gas atmosphere during PBF-LB. Nevertheless, specimens with increased N-content possessed increased ultimate tensile strength of 625 and 762 MPa (0.069 and 0.22 mass% N, respectively) compared to the unmodified steel with 440 MPa. However, no further analysis such as characterization of the fatigue and corrosion behavior was done.

Based on the given information, the modification of the starting powder seems to be a promising way to achieve a higher defect tolerance against fatigue failure in the PBF-LB/M as-built part. Especially for most of the available alloys for PBF-LB/M, it is still not yet possible to achieve fully dense parts and the generation of process-induced defects will lead to locations for preferred crack initiation. As shown from the literature, the increase of N-content in steels could reduce the criticality of certain defects or allow defects with specific sizes to be present in AM parts as it would be less critical due to increased defect tolerance. However, there is a lack of investigations regarding the influence of the strengthening mechanisms in PBF-LB/M on the fatigue behavior.

In this work, 316L stainless steel is modified in a way that maximum solubility is not exceeded but significant amount of nitrogen is induced in the steel. The goal is to characterize the influence of the increased N-content on the microstructure and the defect tolerance by not aiming for fully dense parts but parts with defects in terms of typical lack of fusion porosity. The microstructure of the manufactured specimens is extensively characterized and, additionally, different fatigue tests are performed to evaluate differences in the fatigue behavior and defect tolerance.

## 2. Experimental Section

### 2.1. Material Proceedings

The austenitic stainless steel powder AISI 316L (X2CrNiMo17-12-2, DIN 1.4404), which was provided by Deutsche Edelstahlwerke GmbH, served as the starting powder for the investigations in this work. N was introduced by solid-state nitriding of the starting powder in a vacuum chamber furnace of type IU 54/1 F from Schmetz GmbH. N uptake took place under an N<sub>2</sub> atmosphere (N<sub>2</sub> partial pressure of 3 bar) at a temperature of 675 °C. Before the powder was nitrided for 6 h under these conditions, the temperature was increased in two time steps of 10 h each. In this way, a sufficiently good vacuum was created before the inlet of the nitrogen gas to prevent strong oxidation during nitriding. The process parameters used were taken from the work of Boes et al.<sup>[16]</sup> in which it was shown that a considerable N-content is established in the powder without causing strong agglomeration phenomena. The N and O

contents of the powders were measured by carrier gas hot extraction using an ONH-200 ELTRA analyzer. At this point, it should be noted in advance that an N-content of 0.61 mass% was introduced by the nitriding process. As this N-content in the nitrided powder (hereinafter referred to as 316L-nit) would greatly exceed the N solubility in the molten steel during PBF-LB/M production, the 316L-nit powder was mixed with the 316L starting powder (N-content of 0.058 mass%) to a target N-content of 0.16 mass% (powder mixture hereinafter referred to as 316L + N). This target content was determined based on the results of Boes et al.<sup>[16]</sup> and thermodynamic equilibrium calculations using ThermoCalc and was subject to the objective of generating the maximum possible N-content at which no N outgassing occurs during PBF-LB/M production (see also Section 2.7).

The 316L-nit was mixed with the initial 316L powder by using a 3D tumble mixer (TURBULA Type T2F) at a rotating speed of  $101 \text{ min}^{-1}$  for 6 min. The proportion of the initial 316L powder and the 316L-nit powder was 82 and 18 mass%, respectively. The targeted N-content of the mixed powder is 0.16 mass%.

## 2.2. Powder Characterization

The particle size distributions of the powders were determined by means of a laser diffraction testing instrument (Malvern Mastersizer 2000, Malvern Panalytical GmbH). The particle morphology was investigated by scanning electron microscopy (SEM) (CAMSCAN CS44). The flowability of the powder was determined by means of Hall flow-testing (funnel opening  $\varnothing 2.5 \text{ mm}$ ) according to ISO 4490:2018. The apparent density was measured according to ISO 697:1981. The tap density of the powder was measured after 1250 tap cycles with a JEL STAV II device (J. Engelsmann AG).

## 2.3. Specimen Manufacturing by PBF-LB

Specimens in the form of near net shaped tensile specimens (Figure 1a) and cuboids were manufactured on the PBF-LB/M system Aconity Mini (Aconity3D GmbH). The cuboids were manufactured horizontally, so that the corresponding tensile axis

of the specimens was perpendicular to the build direction. As part of the work, all specimens were analyzed in the as-built condition. No downstream heat treatment or postprocessing was performed. The cuboids had a dimension of 65 mm (length)  $\times$  10 mm (width)  $\times$  11 mm (height). They were built on a platform of AISI 304 stainless steel with a diameter of 140 mm and without any base plate heating. The process chamber was purged with nitrogen gas with a high purity of 99.99% and an oxygen content in the process chamber lower than 50 ppm could be achieved. Based on a parameter study of the AISI 316L steel (to be published elsewhere), the process parameters for the specimens were determined as follows (Table 1).

For fatigue tests, specimens according to Figure 1b were manufactured by machining the cuboids and the gauge section was additionally polished to remove possible turning marks.

## 2.4. Specimen Preparation and Microstructure Investigations

For microstructural investigations, small pieces of the manufactured cuboids were cut, and the corresponding cross sections with either parallel (XY cross section) or perpendicular view (XZ cross section) with regard to the build direction (BD) were hot embedded ( $180 \text{ }^\circ\text{C}$ ) and successively ground and polished with oxide polishing suspension. Thereafter, the specimens were etched with V2A-etchant and investigated with the optical light microscope Axio Imager (Carl Zeiss AG). Further analysis was done by SEM to obtain high magnification images of the microstructure. The SEM is additionally equipped with a Velocity Pro CMOS sensor (EDAX/AMETEK) for EBSD analysis which was done on the XY and XZ cross sections of the PBF-LB processed 316L and 316L + N. SEM was also used for fractographic analysis

**Table 1.** PBF-LB process parameters for 316L and 316L + N steel.

Laser power [W]	Scan speed [ $\text{mm s}^{-1}$ ]	Spot size [ $\mu\text{m}$ ]	Hatch distance [ $\mu\text{m}$ ]	Layer thickness [ $\mu\text{m}$ ]	Scan strategy	Tilt angle [ $^\circ$ ]	Process gas
250	800	50	100	50	Simple hatching	90	$\text{N}_2$

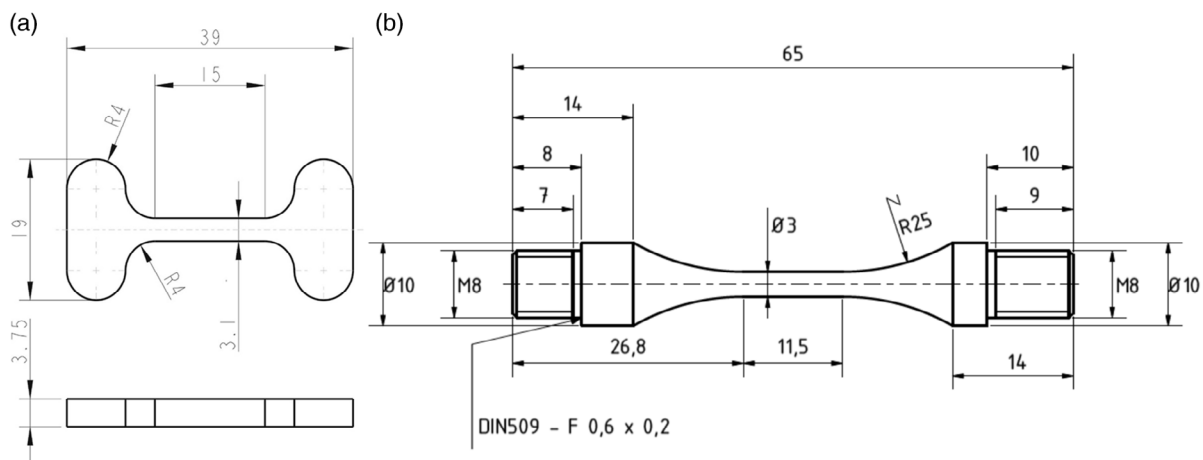


**Figure 1.** Specimen geometry of 316L/316L + N used for a) tensile tests and b) fatigue tests (all numbers in mm).

to gain information about location and size of the crack-initiating defects after fatigue testing. Defect size was measured based on SEM image with ImageJ software (NIH). Furthermore, hardness measurements in terms of Vickers hardness HV10 (loading force of  $F = 98.07$  N) were done on both cross sections on a Dia Testor 3 RC (Otto Wolpert-Werke GmbH) with a minimum of five indents per measurement according to DIN EN ISO 6507-1.

## 2.5. Microfocused Computed X-Ray Tomography

For nondestructive defect detection and to obtain 3D information about the size, location, and shape of defects, microfocus computed tomography ( $\mu$ -CT) was performed with a Nikon XT H 160 system (Nikon Metrology) equipped with a tungsten filament and a real-time detector. For the investigations, the gauge section of randomly selected fatigue specimens (Figure 1b) with 3 mm diameter was scanned. The small cross section of the specimens ensures that it is fully penetrated by the X-Rays. Additionally, a high resolution in terms of voxel size can be achieved. Scanning parameters and achieved resolution can be found in Table S1, Supporting Information. The reconstructed 3D volume was subsequently analyzed by VGStudioMax 3.2 using the VGEasyPore algorithm.

## 2.6. X-Ray Diffraction Measurements

To investigate the phases existing in the PBF-LB/M fabricated components, X-Ray diffraction (XRD) patterns of the two steels were recorded using a Bruker D8 Advance system (Bruker Corp.). The input radiation was Cu  $K\alpha$  radiation with a wavelength of 1.5406 Å. The setup corresponded to the Bragg–Brentano geometry, with which a  $2\theta$  range of 30–90° was successively recorded. The step size was 0.02° and a measuring duration of 10 s was selected per step. In this way, a high resolution was generated, which also allows the detection of phases that may be present in lower concentrations. During the experiment, the specimens rotated around their vertical spatial axis so that the entire specimen surface contributed to the experiment. The examined specimen area corresponded to the middle cut surface, parallel to the buildup direction. The preparation included the cutting of the cubes and subsequent polishing using SiC particle suspension (3 to 1  $\mu$ m). After the experiment, the X-Ray patterns were analyzed by the DIFFRAC.EVA software.

## 2.7. Thermodynamic Calculations

In order to determine the temperature-dependent N-content in the liquid phase of the investigated steel X2CrNiMo17-12-2, CALPHAD calculations were carried out using the ThermoCalc software (version 2021b). The thermodynamic data were taken from the TCFe10 database, and the phases LIQUID (liquid phase), FCC\_A1#1 ( $\gamma$ -Fe), BCC\_A2 ( $\alpha$ - $\delta$ -Fe), FCCA1#2 (monocarbides), HCP ( $M_2(C,N)$ ), M23 ( $M_{23}C_6$ ), M7 ( $M_7C_3$ ), CEM ( $Fe_3C$ ), SIGMA (sigma phase), and LAV (Laves phase) were considered in the simulations. The system size was 1 mol. Moreover, a nitrogen pressure of 1.03 bar was used, which corresponded to the pressure modalities during PBF-LB/M process.

## 2.8. Tensile Testing

The quasistatic mechanical properties were characterized by tensile tests according to DIN EN ISO 6892-1 at room temperature. For this purpose, a ZwickRoell Z100 tensile testing machine (ZwickRoell GmbH & Co. KG) was used. The crosshead speed was 0.5 mm min<sup>-1</sup>. The elongation was determined by the displacement of the traverse. The preparation of the specimens included the grinding of the surface with SiC paper (1000 mesh). Five tensile specimens (Figure 1a) per material were investigated.

## 2.9. Fatigue Testing

For the characterization of the fatigue behavior at room temperature, multiple amplitude tests (MAT) as well as constant amplitude tests (CAT) were performed on a servohydraulic testing system Schenck PSB100 (100 kN load cell, Instron 8800 controller) at  $f = 20$  Hz (MAT) and 10 Hz (CAT) under constant tensile mean stress (load ratio  $R = 0.1$ ). MAT is a short time procedure to obtain information about the fatigue behavior by additionally measuring the material's reaction<sup>[21]</sup> which was already successfully used for different PBF-LB materials.<sup>[19,22]</sup> In this case, stress–strain behavior was measured with a tactile extensometer ( $l_0 = 10$  mm). By that, plastic strain amplitude  $\epsilon_{a,p}$  and total strain amplitude  $\epsilon_{a,t}$  can be used to describe the mechanical material reaction in every step as well as with increasing stress after each step. Detailed information of the stress levels can be found in the results. MAT started at a maximum stress of  $\sigma_{\max, \text{start}} = 200$  MPa (approximately 40% yield strength) at which no fatigue damage is expected. The step length was  $\Delta N = 1E4$  after which the maximum stress was increased by a step size of  $\Delta\sigma_{\max} = 20$  MPa which was repeated until fracture of the specimen. Based on the results of MATs, the CATs were performed at maximum stresses between 320 and 520 MPa.

## 3. Results and Discussion

### 3.1. Characterization of the Powder Particles used for PBF-LB/M

The chemical compositions of the powders considered in this work are shown in Table 2. As already mentioned in Section 2.1, an N-content of 0.61 mass% was introduced by nitriding. It was also described that this content would greatly exceed the N-solubility in the melt during the PBF-LB process, which according to Boes et al.<sup>[16]</sup> would lead to outgassing of N in the melt and, thus, to gas pore formation. For this reason, a powder mixture of nitrided steel powder and starting steel powder was prepared. During powder mixing, a target N-content of

**Table 2.** Chemical compositions of the respective powders determined by optical emission spectrometry in mass%. N and O were determined separately by hot carrier gas extraction (O is given in ppm).

Powder	State	C	Cr	Mn	Si	Ni	Mo	N	O	Fe
316L	Initial	<0.02	16.6	0.65	0.75	12.4	2.3	0.058	355	bal.
316L-nit	Nitrided	<0.02	16.6	0.65	0.75	12.4	2.3	0.610	410	bal.
316L + N	Mixed	<0.02	16.6	0.65	0.75	12.4	2.3	0.161	377	bal.

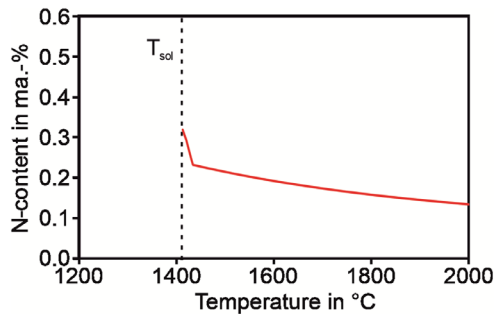


**Figure 2.** Calculated N-solubility in the melt determined by CALPHAD method depending on the temperature.

0.16 mass% was targeted, which was based on thermodynamic calculations. The N-solubility in the steel's melt determined using the CALPHAD method is shown in **Figure 2**. At the solidus temperature of 1414 °C, a N-content of the melt of 0.32 mass% is expected, which decreases with increasing temperature down to 0.135 mass% at a temperature of 2000 °C. Boes et al.<sup>[16]</sup> used similar calculations for linking the N solubility of 316L steel with the tendency to the formation of gas pores caused by exceeding N solubility in the melt during PBF-LB processing. In their work, a N-content of 0.27 mass% led to pronounced gas pore formation during PBF-LB while an initial N-content of 0.065 mass% was low enough to prevent this outgassing phenomenon. Based on these investigations and the thermodynamic calculations in **Figure 2**, the target N-content of 0.16 mass% represents a content that can lead to improvements in the mechanical and chemical properties without showing outgassing phenomena during PBF-LB. The N-content of 0.161 mass% of the powder mixture 316L + N (see **Table 2**) indicates that the mixing of the 316L and 316L-nit powder was successful.

The micrographs of the initial 316L powder are shown in **Figure S1a**, Supporting Information. The powder shows many particles in irregular shape and many satellite particles. Further investigations on the 316L-nit and the mixed powder 316L + N (not shown here) revealed that the nitriding and mixing processes do not have any influence on the particle morphology.

The initial 316L powder, the 316L-nit powder, and the 316L + N powder mixture also reveal similar particle size distribution (see **Figure 3**). The main particle size parameters  $d_{10}$ ,  $d_{50}$ , and  $d_{90}$  are given in **Table 3**. All the powders possess a relatively large particle size. The median particle diameter is about 45  $\mu\text{m}$ . There is only a small number of fine particles (smaller than the nominal lower fraction limit of 20  $\mu\text{m}$ ) present in the powders.

The polished section of the 316L powder particles is presented in **Figure S1b**, Supporting Information. Only a small amount of porosity has been found inside the powder particles. The particle surface of the 316L and the 316L-nit powder was examined by SEM and the results are shown in **Figure 4a,b**. Very fine precipitates were observed at the particle surface of the 316L-nit powder indicated by the red arrows in **Figure 4b**. They are most likely M(C,N) nitrides, which are formed by the uptake of nitrogen into the steel during gas nitriding.<sup>[18]</sup> In addition to precipitate formation at the particle surface, the dendritic microstructure

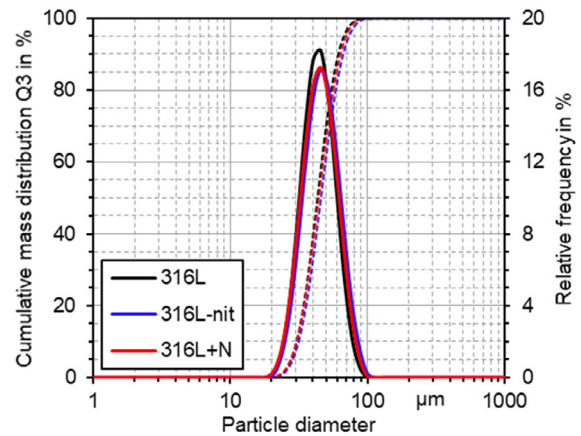


**Figure 3.** Particle size distribution of the initial 316L powder, the 316L-nit powder, and the mixed powder 316L + N.

**Table 3.** Properties of the different conditions of the 316L powder particles.

Powder	Unit	Initial powder 316L	316L-nit	316L + N
Particle size $d_{10}$	$\mu\text{m}$	30.5	31.4	30.3
Particle size $d_{50}$	$\mu\text{m}$	43.3	46.0	44.4
Particle size $d_{90}$	$\mu\text{m}$	61.3	67.4	64.5
Flow time ( $\varnothing 2.5 \text{ mm}$ )	$\text{s } 50 \text{ g}^{-1}$	16.0	16.5	18.0
Apparent density	$\text{g cm}^{-3}$	4.35	4.09	4.18
Tap density	$\text{g cm}^{-3}$	4.76	4.76	4.76

in the initial 316L powder was remarkably modified during the nitriding process as shown in **Figure 4c,d**. The heating and accelerated diffusion under nitriding conditions led to the formation of interdendritic nitrides which also caused a more intense etching in this region.<sup>[16]</sup>

The flow property and the packing density of the respective powders are listed in **Table 3**. They all show good flowability and similar apparent density. As many particles have an irregular shape and many satellite particles, which usually impairs powder flowability, the good flowability of the powders is probably associated with the relatively large particle size range.

### 3.2. Influence of N-Addition on the Microstructure and Process-Induced Defects

Optical microscopy reveals the typical PBF-LB microstructure consisting of clearly visible melt pools in XZ cross section (**Figure 5a,c** and laser scan tracks in XY cross section **Figure 5b,d**) in both investigated materials, respectively. For a better overview, BD is additionally marked. Especially in XZ cross section, grain growth along Z-axis in BD is visible with columnar grains growing through the melt pool boundaries along the temperature gradient during PBF-LB. In XY cross section, the scan strategy is noticeable as scan direction was rotated by 90° after each layer.

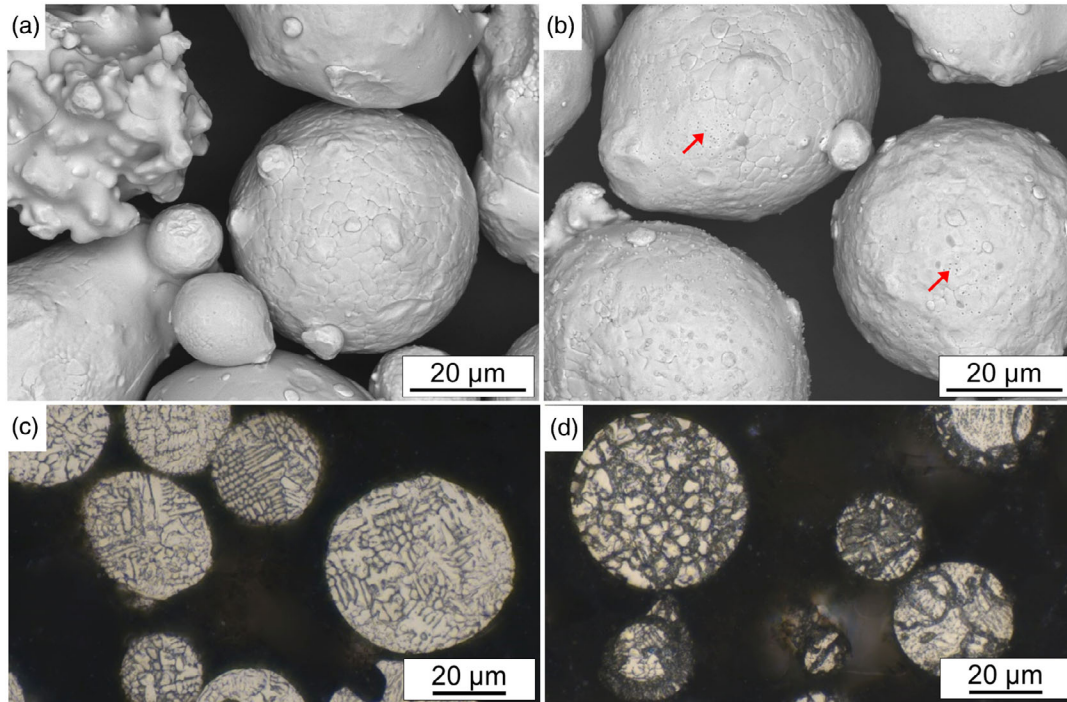


**Figure 4.** SEM (BSE) micrographs of the particle surface of the 316L powder a) before and b) after gas nitriding (red arrows point at nitrides); etched cross sections of the powder particles c) 316L and d) 316L-nit.

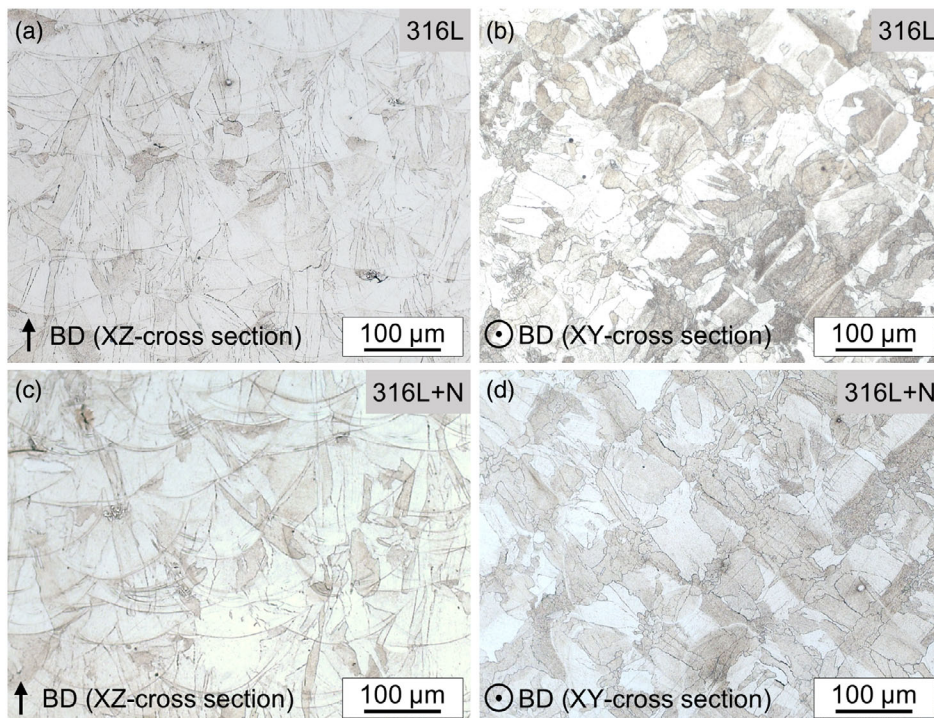


**Figure 5.** Etched microstructure by optical microscopy of a) XZ cross section and b) XY cross section of 316L and c) XZ cross section and d) XY cross section of 316L + N; BD: build direction.

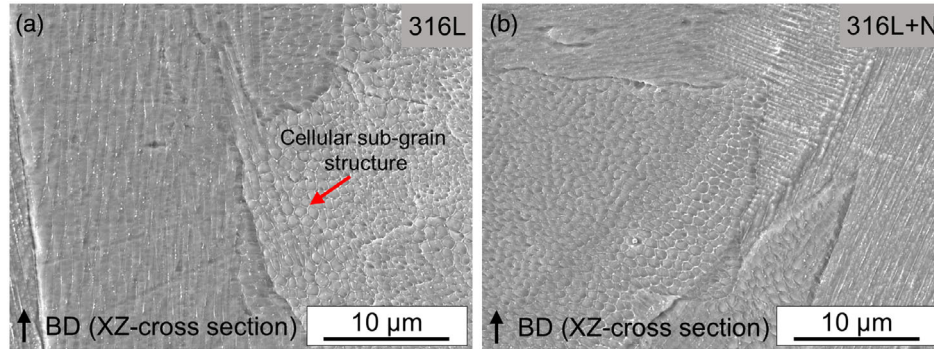


**Figure 6.** SEM images with cellular subgrain structure of XZ cross section of a) 316L and b) 316L + N.

At higher magnifications in SEM, the cellular subgrain structure in terms of equiaxed and columnar dendrites can be identified (see **Figure 6**). The orientation of this structure is mainly based on the heat flow direction and rapid solidification<sup>[23]</sup> which is visible in the XZ cross section of 316L in **Figure 6a** where a tilt and elongation of the cells in not only the BD but also in the direction of other melt pools or grains is present. Deviation of the cell structure can also vary in neighboring grains as shown in **Figure 6b** for the 316L + N. Based on the literature, the interdendritic regions are enriched with heavier elements, such as Mo and Cr, due to microsegregation phenomena upon solidification. Furthermore, these regions are known to exhibit an increased dislocation density as described by Wang et al.<sup>[5]</sup> No significant influence of the N-content on the microstructure can be found in OM or SEM images. Especially the absence of precipitates in the 316L + N specimens has to be mentioned, as nitride formation becomes more likely with increasing N-content. This finding is in accordance with the observations made by Boes et al.,<sup>[16]</sup> and is likely to be associated with the high cooling rates during PBF-LB preventing pronounced precipitation processes. Furthermore, it is clear that N addition, which is not exceeding the calculated maximum N solubility, **Figure 2**, does not lead to N outgassing and the development of structural defects such as spherical gas pores.

Hardness measurements revealed a pronounced hardness increase in both XY and XZ cross sections (**Table 4**) with increasing N-content. The increased N-content leads to an approximately 11-14% higher hardness compared to the 316L steel. Additionally, slightly higher hardness can be found when the hardness is measured perpendicular to the build direction (XZ cross section). The hardness measured in this work is lower compared to the raw and interstitially alloyed 316L with 0.3 mass% N with 267 and 305 HV0.1, respectively, as reported by Valente et al.<sup>[20]</sup> which can be explained by using different test forces (HV0.1 compared to HV10 in this work) as well as having almost twice the amount of N as the

**Table 4.** Results of hardness measurements on 316L and 316L + N cross sections.

	Hardness HV10	
	316L	316L + N
XY cross section	204 ± 4	230 ± 5
XZ cross section	214 ± 13	245 ± 6

316L + N in this work. Nevertheless, the absolute hardness increase of  $\Delta HV$  is quite similar. Hardness values as reported by others<sup>[24]</sup> are very similar to the hardness of the 316L in this work.

Investigations in terms of EBSD scans (**Figure 7a–d** reveal the typical PBF-LB microstructure with visible melt pools or laser scan tracks as it was already shown in the light optical microscopy images (see **Figure 5**) including the epitaxial grain growth through individual melt pools and layers in **Figure 7a,c**. The rotational scan strategy leads to a less textured microstructure as normally a high texture would be expected due to the preferred epitaxial growth<sup>[25–27]</sup> and change direction of local temperature gradient.<sup>[28]</sup> Additionally, slightly different orientation inside most of the grains can be found which can be correlated with low angle grain boundaries or stress compensation.<sup>[27]</sup> Furthermore, the EBSD shows a slight variation in grain orientation in individual grains identifiable by the color gradient.

Based on XRD measurements phase analysis shown in **Figure S2**, Supporting Information, an almost fully austenitic phase composition as exclusively the reflections of the austenitic phase can be identified. This is in correspondence with other findings.<sup>[23,29]</sup> This fully austenitic phase constitution is a result of the high solidification and cooling rates prevailing in the PBF-LB process. On the one hand, these favor primary austenitic solidification due to kinetically more favorable formation of austenite compared to ferrite<sup>[30]</sup> and, on the other hand, prevent ferrite formation at the cell boundaries due to microsegregation of Cr and Mo as observed for example in the context of additive manufacturing by direct energy deposition (DED-LB).<sup>[31]</sup> With regard to the primary solidification of austenite, the influence of nitrogen is estimated to be low in this work. N additionally stabilizes the austenitic phase, which only further supports the already austenitic phase constitution, which was seen for the 316L steel with less N.

In the results of  $\mu CT$  scans, a considerable number of defects in the gauge section of the specimens can be found. In total, PBF-LB leads to 0.71% and 0.56% porosity for the 316L and 316L + N specimen in **Figure 8a–d**, respectively, based on  $\mu CT$  evaluation of the defects. Highest value of defect size in terms of projected defect size perpendicular to the later load direction along the specimen axis were  $\sqrt{\text{area}} = 456$  and  $348 \mu m$  for the 316L and 316L + N specimens shown in **Figure 8**, respectively. Almost all detected defects seem to have

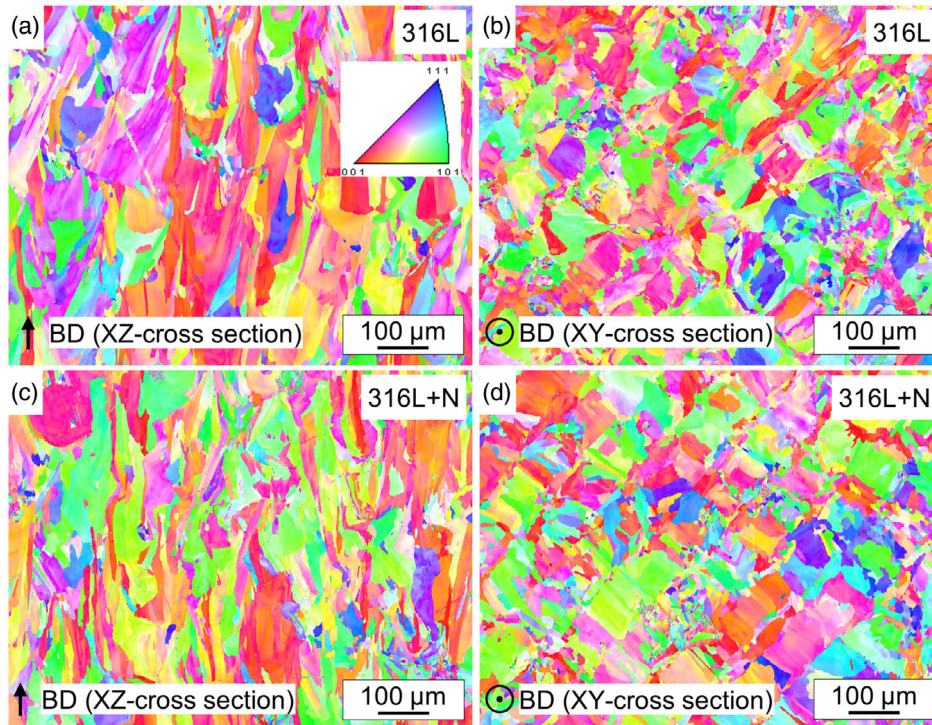


**Figure 7.** Results of EBSD scans (IPF) of a) 316L XZ section; b) 316L XY section; c) 316L + N XZ section; and d) 316L + N XY section.

a quite aspherical flat and elongated shape with a thickness reaching higher than the individual layer size in the process which indicates that no gas porosity was induced during processing as can be seen in Figure 8c,d for the 316L + N specimen.

In addition, a comparison of the N-content of the powders and specimens built using PBF-LB/M (see Table 5) shows that there is negligible decrease in N-content in the 316L + N material. In the 316L material, the specimens also absorb approximately 0.01 mass% N from the process gas during the manufacturing process. This supports the conclusion that solubility of N was not exceeded during PBF-LB. Regarding the 316L + N steel, just a slight decrease in the N-content of 0.003 mass% after PBF-LB processing is observable. In contrast, for the 316L steel, there was an increase in N-content of 0.014 mass% during PBF-LB processing, which is attributed to N uptake from the process atmosphere ( $N_2$ ). At this point, it should be recalled which reference points were used to determine the target N-content of 0.16 mass% in the powder. As shown before, thermodynamic calculations and the results of Boes et al.<sup>[16]</sup> were considered. The absence of spherical gas pores and the only slightly lower N-content of the 316L + N components compared to the 316L + N powder (see Table 5) indicate that this assumption is expedient.

### 3.3. Mechanical Properties

Figure S3, Supporting Information, shows representative stress–strain curves of both steels 316L and 316L + N in the PBF-LB-manufactured condition. The associated mechanical parameters (mean values) such as yield strength (YS), ultimate tensile strength (UTS), and the elongation at fracture (A) can

be seen in Table 6. The YS of 316L + N is about 80 MPa and the UTS about 60 MPa higher compared to 316L steel. The elongation at fracture of steel 316L + N, with a value of 42.4%, is about 6% lower than that of 316L. In summary, nitrogen has led to a significant increase in strength and a slight decrease in elongation at fracture. The increase in strength, which is consistent with the hardness measurements already shown in chapter 3.2, is a result of solid solution strengthening associated with interstitially dissolved N. Gavriljuk et al.<sup>[32]</sup> reported that interstitially dissolved nitrogen atoms act as obstacles for dislocations leading to an overall increased strength. The microstructure analysis in Section 3.2 revealed a mainly austenitic microstructure. Precipitates such as nitrides were not detected. For this reason, it can be concluded that all N introduced is dissolved interstitially in the austenitic lattice leading to the observed strength increase. These observations correspond to the results of Boes et al.,<sup>[16]</sup> which also suggested an N-rich precipitation free microstructure in PBF-LB-built nitrogen containing 316L steel. Also, in the aforementioned work, an increased strength with increasing N-content was detected, which is also in line with the results in the present work. In principle, it is known that the stainless steel's increase in strength associated with the addition of N is not accompanied by a considerable deterioration in ductility. This phenomenon is a result of the influence of N on the bonding character in the iron lattice. N acts as an electron donor leading to an increase of free electrons which promotes the metallic bonding character.<sup>[32]</sup> This effect simultaneously contributes to the steel's ductility in a considerable manner. The results in the present work show a decrease of 12% from 48.2% to 42.4% in the elongation at



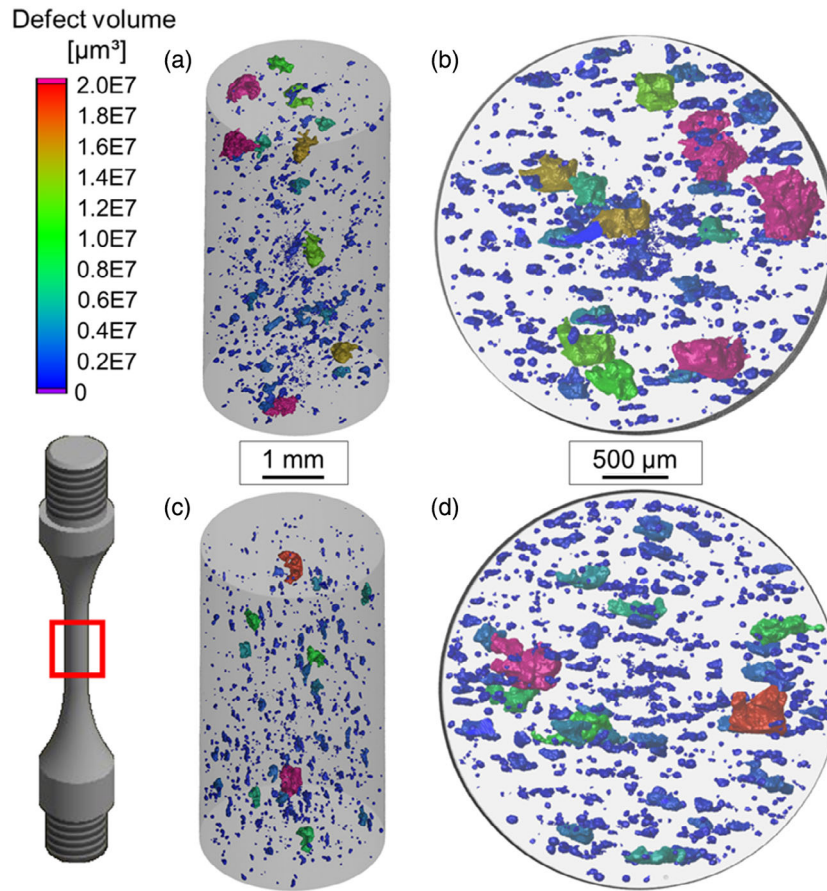


**Figure 8.** Results from  $\mu$ CT scans with defect distribution in 316L a) diagonal above view; b) top view; and in 316L + N c) diagonal above view and d) top view.

**Table 5.** Results of nitrogen measurements on 316L and 316L + N before and after PBF-LB processing determined using carrier gas hot extraction.

	N-content in mass%	
	Powder	PBF-LB
316L	0.058	0.072
316L + N	0.161	0.158

**Table 6.** Results of tensile tests.

Material	Yield strength YS [MPa]	Ultimate tensile strength UTS [MPa]	Elongation at fracture A [%]
316L	490 ± 19	656 ± 16	48.2 ± 3.6
316L + N	569 ± 11	714 ± 16	42.4 ± 6.9

fracture, while the YS and UTS increase about 16% and 8%, respectively, with a higher N-content in the 316L steel confirming the described mechanism known from the literature.

The results of MAT are shown in **Figure 9**. In general, similar material behavior under cyclic loading in terms of change in  $\epsilon_{a,t}$  and  $\epsilon_{a,p}$  can be found. Whereas at low maximum stress a linear

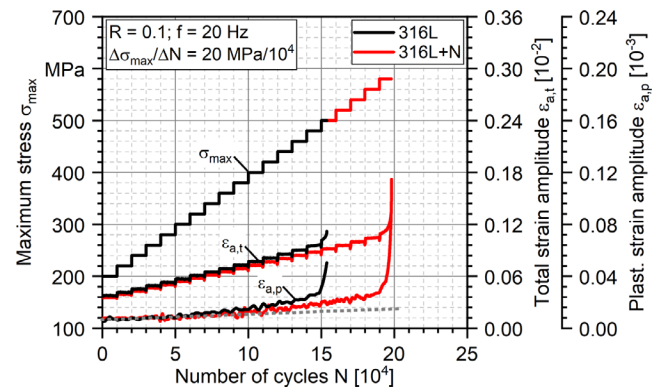


**Figure 9.** Results of multiple amplitude tests including material reaction in terms of plastic and total strain amplitude for 316L and 316L + N.

trend especially in  $\epsilon_{a,p}$  can be found, this is no longer the case at  $\sigma_{max} = 360$  MPa for 316L and  $\sigma_{max} = 420$  MPa for 316L + N, respectively. By that, it is already possible to say that the effect of the increased amount of N can already be found by a shifted first significant material reaction to higher  $\sigma_{max}$ , similar to the results found in tensile tests (Table 6). Furthermore, both specimens failed with visible increase of  $\epsilon_{a,p}$  which can be correlated

to cyclic softening as well as unstable crack growth rate in the last step indicated by the increase in  $\epsilon_{a,t}$ . In general, austenitic steels can show high ductility not only under quasistatic but also under fatigue loading. Stern et al.<sup>[22]</sup> did MAT of 316L under  $R = -1$  (tension–compression, fully reversed loading) and found good correlation with results from MAT and later CAT when comparing the influence of different build directions on the fatigue behavior. The results also showed high ductility and exponential increase of  $\epsilon_{a,t}$  and  $\epsilon_{a,p}$  shortly before failure. The stress in the last step of MAT of 500 and 580 MPa for 316L and 316L + N, respectively, is also very similar to the YS from tensile tests (Table 6).

Results of tests at constant  $\sigma_{max}$  are shown in **Figure 10** in terms of a classical S–N curve fitted by Basquin Equation (1) with  $\sigma'_f$  [MPa] as fatigue strength coefficient and  $b$  [-] as fatigue strength exponent.

$$\sigma_{max} = \sigma'_f (N_f)^b \quad (1)$$

The fatigue life is significantly higher at high stresses for 316L + N where higher yield stress seems to have a big influence on the number of cycles to failure. At lower stresses, this effect seems to become neglectable as both curves intersect at the lowest tested stress of  $\sigma_{max} = 320$  MPa. The Basquin fit reveals an apparent high difference in fatigue behavior of the two investigated materials as especially the fatigue exponent  $b$  of the PBF-LB 316L is quite high compared to conventionally manufactured 316L as described by Puchi-Cabrera et al.<sup>[33]</sup> Their findings are more comparable to the results of 316L + N with  $\sigma'_f = 5750$  MPa and  $b = -0.212$  while for 316L + N it is 6760 MPa and  $-0.2243$ , respectively. However, the results should only be discussed after considering the outcome of the fractography as results from ref. [33] were performed on specimens with a hemispherical notch at the surface. Compared to other fatigue results, the fatigue strength of PBF-LB 316L at  $N = 10^6$  reported by Spierings et al.<sup>[34]</sup> for both machined and polished specimens was estimated at approximately 320 MPa based on the given S–N curves ( $\sigma_{max}$ ). The results in Figure 10 indicate a similar but slightly lower fatigue strength for both 316L and 316L + N and have to be complemented by further tests in the future.

Investigations of the fractured surface by SEM reveal that all specimens under cyclic loading failed from LoF defects near or in direct contact with the surface. Shape and size of the LoFs is

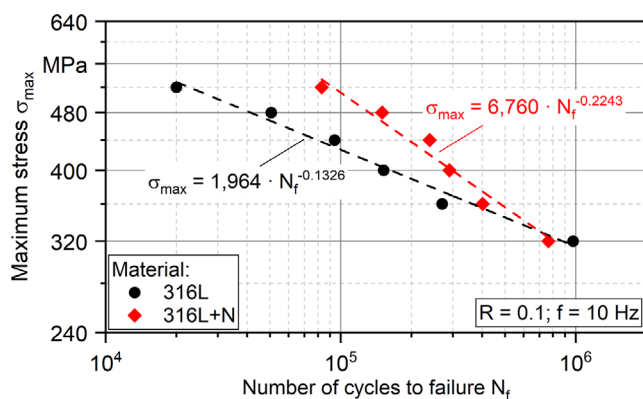


**Figure 10.** Results of constant amplitude tests in form of Woehler curves for the 316L and 316L + N specimens.

similar to the results from  $\mu$ CT. For a better comparison, fractured surfaces of both batches with similar fatigue life are depicted in **Figure 11**. As further shown in Figure 11a,b, crack initiation for the 316L took place directly at the LoF which is positioned directly at the surface of the specimen. Similar to that, the fatigue crack shown in Figure 11c,d for 316L + N started from a LoF which was positioned slightly below the specimen's surface. Inside both defects, un- and partially melted powder particles can be found. For 316L, defects with sizes between 134 and 475  $\mu$ m were crack initiating, while for 316L + N it was in the range of 187–391  $\mu$ m. Size and shape of the defects correspond quite well with the findings of  $\mu$ CT as shown in Figure 8b,d.

The surface around the defects showed no signs of fisheye-like characteristics and, thus, no smooth but a more striated surface morphology. This finding has also been reported by Andreau et al.<sup>[35]</sup> for regular PBF/LB 316L under fatigue ( $R = 0.1$ ) and is related to intergranular crack propagation. They state that this is most probably caused by a weakening of the grain boundaries by ambient oxygen or hydrogen.

Based on the fatigue results and the difference in fatigue strength exponent, it appears that either the mechanism of crack initiation and/or crack propagation is substantially changed by the higher N-content or that even other aspects have to be considered. Fractography already revealed that the scatter in size and shape of crack-initiating LoF defects is quite high and, in the introduction, it was already stated that different defect sizes lead to different S–N curves.<sup>[9]</sup> So, it is possible that due to statistical reasons the seemingly different slopes of the S–N curves in this work and the supposed difference in failure mechanism could be a misinterpretation of the limited number and the corresponding high scatter of data points.<sup>[36]</sup> Especially in AM, where specimens can be more expensive or the amount of powder is limited due to specific modifications, the number of available specimens can be small. However, the characterization of the fatigue behavior is essential for a safe design of AM parts and, thus, cannot be neglected.

To exclude the possibility that the higher fatigue life of the 316L + N specimens is only based on possibly smaller defects tested at the individual stresses when compared to the direct partner of 316L, **Figure 12a** was set up to visualize the defect size based on fractography by SEM at the corresponding  $\sigma_{max}$ . Unexpectedly and unbeknown, specimens of both batches tested at stresses of  $\sigma_{max} = 440$  MPa and higher had the biggest crack-initiating defects with  $\sqrt{\text{area}} > 300$   $\mu$ m compared to the stresses lower than 440 MPa. Additionally, except for  $\sigma_{max} = 440$  and 260 MPa, specimens from 316L always had the bigger crack-initiating defect. A first indicator for a better fatigue behavior of the 316L + N can be found in the number of cycles to failure of both batches at  $\sigma_{max} = 440$  MPa where the defect sizes were almost identical, namely, 368 and 391  $\mu$ m for 316L and 316L + N, respectively. Batch 316L + N showed slightly higher fatigue life of  $N_f = 1.53 \times 10^5$  compared to  $1.35 \times 10^5$  of 316L (Figure 10). As the size of the crack-initiating defect is known, the difference of approximately 13% should be completely relatable to the increased N-content as fatigue life is significantly dominated by the size of the present defect(s).<sup>[11]</sup> In general, the defect sizes in this work are similar or bigger compared to other results<sup>[24,37,38]</sup> where either keyhole pores or LoFs were crack initiating in fatigued PBF/LB 316L with minimum defect sizes of less

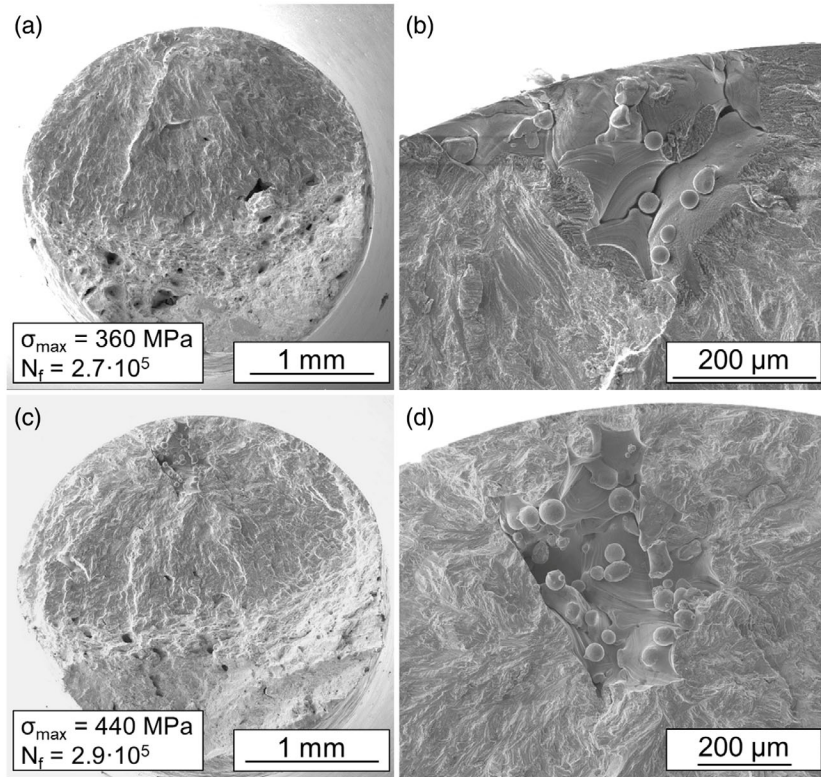


**Figure 11.** Fractured surfaces of: 316L a) overview and b) crack-initiating defect; and 316L + N c) overview and d) crack-initiating defect.

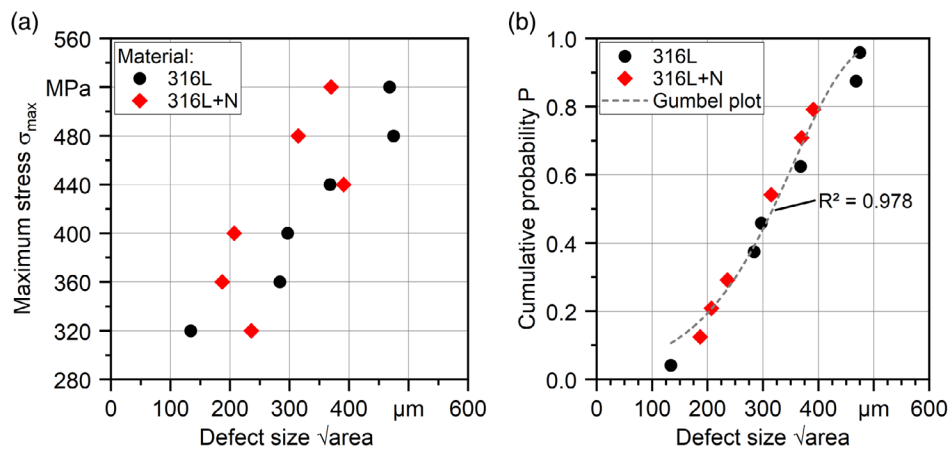


**Figure 12.** a) Comparison of maximum stress and size of crack-initiating defect  $\sqrt{\text{area}}$ ; b) Gumbel plot of crack initiating defects.

than 100  $\mu\text{m}$  and maximum defect sizes of up to 370  $\mu\text{m}$ , respectively. Additionally, **Figure 12b** shows that the crack-initiating defect sizes follow an extreme value distribution in terms of the Gumbel distribution (Equation (2)),<sup>[39]</sup> which is able to describe extreme defects in many applications,<sup>[36]</sup> e.g., nonmetallic inclusions in steels.<sup>[40]</sup> Here,  $\lambda$  and  $\delta$  are the location and scale parameters, respectively. Cumulative probability was estimated by Equation (3) with specimen number  $i$  and total number of specimens  $n$ . This is also important to consider as statistic of

extremes can be used for quality control in the future<sup>[41]</sup> as fatigue strength distribution or failure probability can be estimated.<sup>[36]</sup>

$$P = 1 - \exp \left[ -\exp \left( \frac{\sqrt{\text{area}} - \lambda}{\delta} \right) \right] \quad (2)$$

$$P = \frac{i - 0.5}{n} \quad (3)$$

Due to the aforementioned effect of defects and the number of specimens tested in this work, the resulting slopes of the Basquin equation in Figure 10 of 316L + N compared to 316L cannot be used to describe the fatigue behavior of the material in a general way. In the literature, different diagrams can be created to consider load and defect size such as  $\Delta K-N_f$  curves<sup>[42,43]</sup> or the modified S-N curve proposed by Murakami<sup>[9]</sup> which were originally set up to describe the influence of nonmetallic inclusions on the fatigue behavior. Shiozawa et al.<sup>[44]</sup> also used  $\Delta K-N_f/\sqrt{\text{area}}$  curves to show the dependency of defect size and fatigue life. In a first attempt in **Figure 13**, a modified S-N curve, a so-called S- $N_f/\sqrt{\text{area}}$  curve, is plotted. Here, for each data point, the size of the crack-initiating defect in terms of its  $\sqrt{\text{area}}$  was considered to calculate a defect-size normalized fatigue life ( $N_f/\sqrt{\text{area}}$ ) to include the influence of the defect size on the fatigue life.

By that, both curves seem to align more parallel except for the results at 320 MPa where the crack-initiating defect size in the 316L specimen was almost half the size of the one in the 316L + N specimen. Except for the two aforementioned data points, the improved fatigue behavior introduced by the higher N-content can be described without the caused scatter in fatigue life caused by the different sizes of the crack-initiating defects in terms of a comparable slope.

A more established plot of the results can be achieved by setting up a modified S-N curve as described by Murakami.<sup>[9]</sup> By calculating the fatigue strength  $\sigma_w$  (Equation (4)) for every batch and specimen with the measured defect size, the ratio of fatigue strength to applied stress amplitude  $\sigma_a$  at  $R=0.1$  the diagram in **Figure 14** can be achieved. Based on ref. [45],  $\alpha$  is defined as  $0.226 + HV \times 10^{-4}$ .

$$\sigma_w = 1.43 \frac{(HV + 120)}{(\sqrt{\text{area}})^{1/6}} \left[ \frac{1 - R}{2} \right]^\alpha \quad (4)$$

As the different material condition or microstructure is considered in this model in terms of the hardness HV, no significant deviation of the data points is expected which holds true as can be seen in Figure 14. The higher hardness of the 316L + N leads to higher  $\sigma_w$  when the same defect size is considered in both 316L and 316L + N. As y-axis is based on  $\sigma_a/\sigma_w$  this ratio would decrease and can only be counteracted with an increasing fatigue

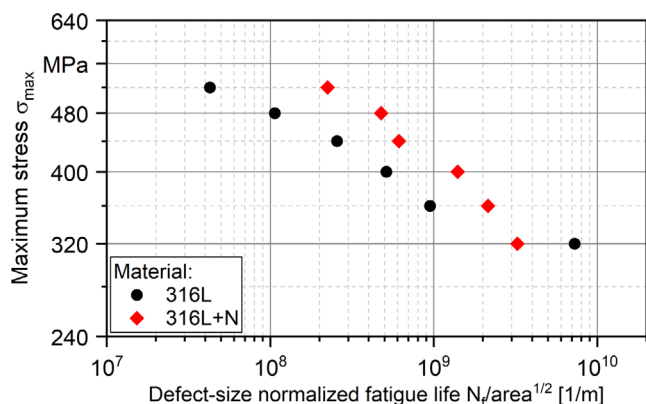


**Figure 13.** Modified S- $N_f/\sqrt{\text{area}}$  curve of 316L and 316L + N steel.

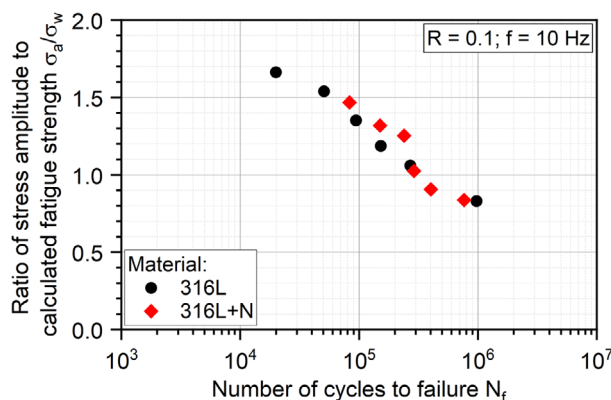


**Figure 14.** Modified S-N diagram according to Murakami<sup>[9]</sup> for the 316L and 316L + N steel.

life to overlap again with the results of 316L. At around 1.2-1.3, the results of 316L + N perform even better than the 316L. Additionally, the specimens tested at  $\sigma_{\text{max}} = 320$  MPa which corresponds to  $\sigma_a/\sigma_w = 0.85$  fit much better in the normalized data points. It can be stated that the solid solution strengthening of the 316L + N specimens leads to improved mechanical strengths which also holds true for the fatigue behavior. It can also be said that the achieved higher hardness is a suitable microstructural value to characterize this effect by using the Murakami approach.

## 4. Conclusion and Outlook

In this work, an increased content of nitrogen in 316L stainless steel was optimized for PBF-LB manufacturing to achieve improved mechanical properties in the processed steel. The N-content was increased by nitriding the initial powder and mixing the nitrided and initial powder to achieve an N-content of 0.16%. No degassing of  $N_2$  or formation of nitrides in the typical PBF-LB microstructure could be found. Hereby, the hardness and ultimate tensile strength could be improved from 214 to 245 HV10 and from 656 to 714 MPa, respectively, as the nitrogen was assumed to be fully interstitially dissolved. The defect tolerance was characterized by manufacturing specimens with a porosity of approximately 0.6% where crack initiation occurred at lack of fusion defects. By that, the defect tolerance could be compared in terms of fatigue testing and fractographic investigations to utilize the Murakami approach. The increased nitrogen content could be verified as it can be included in the model by considering the difference in hardness of initial and modified 316L.

In upcoming investigations, the presented results in this work will be complemented by characterizing the corrosion properties and the behavior of the PBF-LB steel under combined corrosion and fatigue loading will be focused.

## Supporting Information

Supporting Information is available from the Wiley Online Library or from the author.

## Acknowledgements

The authors thank the German Research Foundation (Deutsche Forschungsgemeinschaft, DFG) for its financial support within the research project "Mechanism-based assessment of the influence of powder production and process parameters on the microstructure and the deformation behavior of SLM-compacted C + N steels in air and in corrosive environments" (project no. 372290567; WA 1672/30-2, TH 531/20-2, UH 77/12-2).

Open Access funding enabled and organized by Projekt DEAL.

## Conflict of Interest

The authors declare no conflict of interest.

## Data Availability Statement

The data that support the findings of this study are available from the corresponding author upon reasonable request.

## Keywords

AISI 316L, defect tolerance, fatigue behavior, laser powder bed fusion, nitrogen alloying

Received: May 25, 2022

Revised: July 21, 2022

Published online: August 2, 2022

- [1] S. Afkhami, M. Dabiri, S. H. Alavi, T. Björk, A. Salminen, *Int. J. Fatigue* **2019**, 122, 72.
- [2] K. Solberg, F. Berto, *Mater. Des. Process. Commun.* **2019**, 1, 51.
- [3] S. Tammas-Williams, P. J. Withers, I. Todd, P. B. Prangnell, *Sci. Rep.* **2017**, 7, 7308.
- [4] A. Röttger, K. Geenen, M. Windmann, F. Binner, W. Theisen, *Mater. Sci. Eng. A* **2016**, 678, 365.
- [5] Y. M. Wang, T. Voisin, J. T. McKeown, J. Ye, N. P. Calta, Z. Li, Z. Zeng, Y. Zhang, W. Chen, T. T. Roehling, R. T. Ott, M. K. Santala, P. J. Depond, M. J. Matthews, A. V. Hamza, T. Zhu, *Nat. Mater.* **2018**, 17, 63.
- [6] O. Fergani, A. Bratli Wold, F. Berto, V. Brotan, M. Bambach, *Fatigue Fract. Eng. Mater. Struct.* **2018**, 41, 1102.
- [7] B. Blinn, M. Klein, C. Gläßner, M. Smaga, J. Aurich, T. Beck, *Metals* **2018**, 8, 220.
- [8] T. DebRoy, H. L. Wei, J. S. Zuback, T. Mukherjee, J. W. Elmer, J. O. Milewski, A. M. Beese, A. Wilson-Heid, A. De, W. Zhang, *Prog. Mater. Sci.* **2018**, 92, 112.
- [9] Y. Murakami, T. Takagi, K. Wada, H. Matsunaga, *Int. J. Fatigue* **2021**, 146, 106138.
- [10] S. Beretta, S. Romano, *Int. J. Fatigue* **2017**, 94, 178.
- [11] D. Kotzem, S. Kleszczynski, F. Stern, A. Elspaß, J. Tenkamp, G. Witt, F. Walther, *Int. J. Fatigue* **2021**, 148, 106207.
- [12] M. Nyström, U. Lindstedt, B. Karlsson, J.-O. Nilsson, *Mater. Sci. Technol.* **1997**, 13, 560.
- [13] T. Masumura, N. Nakada, T. Tsuchiyama, S. Takaki, T. Koyano, K. Adachi, *Acta Mater.* **2015**, 84, 330.
- [14] W. A. Ghanem, W. A. Hussein, S. N. Saeed, S. M. Bader, R. M. Abou Shahba, *MAS* **2015**, 9, 119.
- [15] V. G. Gavriljuk, *ISIJ Int.* **1996**, 36, 738.
- [16] J. Boes, A. Röttger, L. Becker, W. Theisen, *Addit. Manuf.* **2019**, 30, 100836.
- [17] J. Menzel, W. Kirschner, G. Stein, *ISIJ Int.* **1996**, 36, 893.
- [18] F. Stern, F. Grabienski, F. Walther, J. Boes, A. Röttger, W. Theisen, *Mater. Test.* **2020**, 62, 19.
- [19] J. Boes, A. Röttger, W. Theisen, C. Cui, V. Uhlenwinkel, A. Schulz, H.-W. Zoch, F. Stern, J. Tenkamp, F. Walther, *Addit. Manuf.* **2020**, 34, 101379.
- [20] E. H. Valente, V. K. Nadimpalli, T. L. Christiansen, D. B. Pedersen, M. A. Somers, *Manuf. Lett.* **2021**, 1, 100006.
- [21] F. Walther, *Mater. Test.* **2014**, 56, 519.
- [22] F. Stern, J. Kleinhorst, J. Tenkamp, F. Walther, *Fatigue Fract. Eng. Mater. Struct.* **2019**, 42, 2422.
- [23] K. Saeidi, X. Gao, Y. Zhong, Z. J. Shen, *Mater. Sci. Eng. A* **2015**, 625, 221.
- [24] F. Stern, J. Tenkamp, F. Walther, *Prog. Addit. Manuf.* **2020**, 5, 287.
- [25] N. Nadammal, T. Mishurova, T. Fritsch, I. Serrano-Munoz, A. Kromm, C. Haberland, P. D. Portella, G. Bruno, *Addit. Manuf.* **2021**, 38, 101792.
- [26] J. Suryawanshi, K. G. Prashanth, U. Ramamurty, *Mater. Sci. Eng. A* **2017**, 696, 113.
- [27] M. Godec, Č. Donik, A. Kocijan, B. Podgornik, D. A. Skobir Balantič, *Addit. Manuf.* **2020**, 32, 101000.
- [28] M. J. Uddin, E. Ramirez-Cedillo, R. A. Mirshams, H. R. Siller, *Mater. Character.* **2021**, 174, 111047.
- [29] C. Qiu, M. A. Kindi, A. S. Aladawi, I. A. Hatmi, *Sci. Rep.* **2018**, 8, 7785.
- [30] S. Fukumoto, W. Kurz, *ISIJ Int.* **1999**, 39, 1270.
- [31] P. Bajaj, A. Hariharan, A. Kini, P. Kürnsteiner, D. Raabe, E. A. Jäggle, *Mater. Sci. Eng. A* **2020**, 772, 138633.
- [32] V. G. Gavriljuk, H. Berns, *High Nitrogen Steels*, Springer Berlin Heidelberg, Berlin, Heidelberg **1999**.
- [33] E. Puchi-Cabrera, F. Matínez, I. Herrera, J. Berríos, S. Dixit, D. Bhat, *Surf. Coat. Technol.* **2004**, 182, 276.
- [34] A. B. Spierings, T. L. Starr, K. Wegener, *Rapid Prototyping J.* **2013**, 19, 88.
- [35] O. Andreau, E. Pessard, I. Koutiri, P. Peyre, N. Saintier, *Int. J. Fatigue* **2021**, 143, 105930.
- [36] S. Romano, A. Brandão, J. Gumpinger, M. Gschweil, S. Beretta, *Mater. Des.* **2017**, 131, 32.
- [37] B. Blinn, M. Ley, N. Buschhorn, R. Teutsch, T. Beck, *Int. J. Fatigue* **2019**, 124, 389.
- [38] O. Andreau, E. Pessard, I. Koutiri, J.-D. Penot, C. Dupuy, N. Saintier, P. Peyre, *Mater. Sci. Eng. A* **2019**, 757, 146.
- [39] E. J. Gumbel, *Statistics of Extremes*, Columbia University Press, New York, NY **1958**, <https://doi.org/10.7312/gumb92958>.
- [40] M. Tiryakioğlu, *Mater. Sci. Eng. A* **2009**, 520, 114.
- [41] Y. Murakami, H. Masuo, Y. Tanaka, M. Nakatani, *Procedia Struct. Integrity* **2019**, 19, 113.
- [42] Y. Shimatani, K. Shiozawa, T. Nakada, T. Yoshimoto, *Procedia Eng.* **2010**, 2, 873.
- [43] K. Shiozawa, L. Lu, S. Ishihara, *Fatigue Fract. Eng. Mater. Struct.* **2001**, 24, 781.
- [44] K. Shiozawa, L. Lu, *AMR* **2008**, 44–46, 33.
- [45] Y. Murakami, *Metal Fatigue: Effects of Small Defects and Nonmetallic Inclusions*, 1<sup>st</sup> ed, Elsevier, Amsterdam **2002**, <https://doi.org/10.1016/b978-0-08-044064-4.x5000-2>.